

Lattice Boltzmann Simulations of Multiphase Dielectric Fluids

Élfego Ruiz-Gutiérrez,[†] Andrew M. J. Edwards,[‡] Glen McHale,[†] Michael I. Newton,[‡] Gary G. Wells,[†] Carl V. Brown,[‡] and Rodrigo Ledesma-Aguilar^{*,†}

[†]*Institute for Multiscale Thermofluids, School of Engineering, University of Edinburgh, The King's Buildings, Mayfield Road, Edinburgh EH9 3FB, UK.*

[‡]*SOFT Group, School of Science and Technology, Nottingham Trent University, Clifton Lane, Nottingham NG11 8NS, UK.*

E-mail: rodrigo.ledesma@ed.ac.uk

Abstract

The dynamic effect of an electric field on dielectric liquids is called liquid dielectrophoresis. It is widely used in several industrial and scientific applications, including inkjet printing, micro-fabrication and optical devices. Numerical simulations of liquid-dielectrophoresis are necessary to understand the fundamental physics of the phenomenon, but also to explore situations that might be difficult or expensive to implement experimentally. However, such modelling is challenging, as one needs to solve the electrostatic and fluid dynamics equations simultaneously. Here, we formulate a new lattice-Boltzmann method capable of modelling the dynamics of immiscible dielectric fluids coupled with electric fields within a single framework, thus eliminating the need of using separate algorithms to solve the electrostatic and fluid dynamics equations. We validate the numerical method by comparing it with analytical solutions and previously reported experimental results. Beyond the benchmarking of the method, we

study the spreading of a droplet using a dielectrowetting setup and quantify the mechanism driving the variation of the apparent contact angle of the droplet with the applied voltage. Our method provides a useful tool to study liquid-dielectrophoresis and can be used to model dielectric fluids in general, such as liquid-liquid and liquid-gas systems.

Introduction

When a dielectric fluid interacts with an electric field, its atoms or molecules will respond to the field polarising the medium.^{1,2} This produces a ponderomotive force that acts on the fluid, an effect called liquid dielectrophoresis (L-DEP).³⁻⁵ The ability to accurately control this dielectric force has current potential technological applications, such as inkjet printing,⁶ optical devices,^{7,8} micro-assembly⁹ and electrospinning.¹⁰ One important application of L-DEP is dielectrowetting, which is a novel technique used to control the spreading of a droplet on solid surfaces.^{11,12} This technique is similar to electrowetting since both use an electric field to spread a liquid. However, dielectrowetting differs from electrowetting in that dielectrowetting uses the bound charges from polarisation, as opposed to the free charges of a conducting liquid in electrowetting setups.¹³ Also, dielectrowetting does not suffer from the contact angle saturation observed in electrowetting.¹⁴

Numerical simulations of the dynamics of multiphase fluids coupled with electric fields open the door for a wide range of applications.¹⁵⁻¹⁷ For example, in microfluidic devices, by improving the manipulation of small amounts of liquid with the fine control that electronic devices allow.^{18,19} Moreover, numerical simulations have the potential to inform the design of electrode arrays to induce specific and complex liquid and film morphologies both at fluid-fluid interfaces and for finite volumes of liquids on solids.^{7,12,20} For this reason, several numerical methods have been implemented to study this interaction, for example, finite-element,^{21,22} boundary-element,²³ finite-volume²⁴⁻²⁶ and spectral methods.^{27,28}

Here, we present a lattice-Boltzmann method (LBM) capable of solving the hydrodynamic equations for dielectric fluids in the presence of electrostatic fields. The LBM belongs

to the family of computational fluid dynamics simulations and has gained its reputation for faithfully describing a wide range of phenomena, from rarefied supersonic plasmas to capillary phenomena²⁹ and for its ease of parallelisation.^{30,31} We base our method on the diffuse interface formulation by defining the total free energy of the system³² which includes the capillary and electrostatic contributions.³³ By adopting a modern formulation to the method inspired by spectral methods,²⁷ we endow the LBM with the capacity to include dielectrics. In this way, we improve the efficiency and stability of the method whilst presenting a comprehensive approach to the method. The result is that the hydrodynamic and electrostatic equations are solved within a single method, which alleviates the need of running a separate algorithm concurrently.

This article is organised as follows. In section we set the theoretical framework in which the lattice-Boltzmann simulations are based. In section we describe our numerical method. In section we validate the method against analytical and experimental results to conclude in section .

Governing Equations

Diffuse interface approach to liquid-dielectrophoresis

We consider a two-phase fluid of two perfect dielectric fluids. The mechanical description of the fluid is given by the continuity and Navier-Stokes equations,³⁴ in the incompressible limit they read,

$$\nabla \cdot \mathbf{u} = 0, \tag{1}$$

$$\rho (\partial_t + \mathbf{u} \cdot \nabla) \mathbf{u} = - \nabla \cdot \mathbf{P} + \mu \nabla^2 \mathbf{u} + \mathbf{f}, \tag{2}$$

respectively, where ρ is the mass density of the fluid, \mathbf{u} is the local fluid velocity, \mathbf{P} represents corresponds to the pressure tensor, μ is the dynamic viscosity, and the last term, \mathbf{f} , accounts

for the body forces.

The capillary and dielectric forces that drive the fluid are contained in \mathbf{P} and are derived from the thermodynamic and electric properties of the fluid. We describe the system using a diffuse-interface model where the two phases are identified by a phase field, $\phi = \phi(\mathbf{x})$, which evolves according to another conservation equation, known as the Cahn-Hilliard equation,³⁵

$$\partial_t \phi + \mathbf{u} \cdot \nabla \phi = M \nabla^2 \vartheta, \quad (3)$$

where M is a constant called the mobility and ϑ corresponds to the chemical potential field.

For consistency, we derive the expressions for the pressure and chemical potential from a Helmholtz free energy, \mathcal{F} , of the fluid mixture³⁶ coupled by the electric field

$$\mathcal{F}[\phi, V] = \int_{\Omega} \left[\psi(\phi, \nabla \phi) - \frac{1}{2} \mathbf{D} \cdot \mathbf{E} \right] d^3 \mathbf{x} + \int_{\partial \Omega} \zeta \phi dS. \quad (4)$$

Here, Ω corresponds to the volume occupied by the fluid mixture and it is bounded by $\partial \Omega$. The first integral on the right-hand side of Eq. (4) comprises the energy density of the fluid mixture. It can be broken down into thermodynamic and electric contributions.

For the thermodynamic contribution, to model the free energy density of a binary fluid,³² we define

$$\psi(\phi, \nabla \phi) := \frac{3\gamma}{\sqrt{8}\ell} \left(\frac{1}{4} \phi^4 - \frac{1}{2} \phi^2 + \frac{1}{2} \ell^2 |\nabla \phi|^2 \right), \quad (5)$$

where the $:=$ symbol denotes equal by definition. For a homogeneous mixture ($\nabla \phi = 0$), the free energy density has two minima at $\phi = \pm 1$, indicating the value of the phase field when the two phases are in equilibrium. Due to the term $|\nabla \phi|^2$, the transition between the two phases is smooth, and occurs over a length-scale ℓ , called the interface thickness. This transition has an overall energy cost per unit area, γ , the surface tension. Due to symmetry upon a change of sign ($\phi \leftrightarrow -\phi$), we define the interface to be the manifold where $\phi = 0$, i.e., $\{\mathbf{x} : \phi(\mathbf{x}) = 0\}$.

The electric contribution to the energy of the fluid mixture is given by the following term which is composed of the electric field, \mathbf{E} , and the displacement field, \mathbf{D} . Provided the electric potential,¹ $V(\mathbf{x})$, these are derived by,

$$\mathbf{E} = -\nabla V, \quad \text{and} \quad \mathbf{D} = \varepsilon \mathbf{E} \quad (6)$$

and ε corresponds to the electric permittivity. Here, we have assumed that the fluids are isotropic, linearly polarisable and that the electric permittivity is a scalar function of the phase field, $\varepsilon = \varepsilon(\phi)$. In order to satisfy a prescribed value at the equilibrium of phase coexistence, and basing the variation of the electric permittivity according to the Clausius-Mossotti relation³⁷ we set,

$$\varepsilon(\phi) := 2 \frac{\varepsilon_1 \varepsilon_2 + \varepsilon_0 \varepsilon_1 (1 + \phi) + \varepsilon_0 \varepsilon_2 (1 - \phi)}{4\varepsilon_0 + \varepsilon_1 (1 - \phi) + \varepsilon_2 (1 + \phi)}, \quad (7)$$

where ε_0 , ε_1 and ε_2 are the permittivities of free space, phase $\phi = +1$ and $\phi = -1$, respectively.

The last term on the right-hand side of Eq. (4) corresponds to the interaction energy of the fluid with its boundaries. The constant, ζ , is known as the wetting potential^{38,39} and is related to the equilibrium contact angle, θ_e , by,

$$\zeta(\theta_e) = \frac{3}{2} \gamma \operatorname{sgn}(\pi/2 - \theta_e) [\cos \alpha (1 - \cos \alpha)]^{1/2}, \quad (8)$$

where $\alpha = \frac{1}{3} \arccos \sin^2 \theta_e$.

Once defining the total free energy of the fluid mixture, we can derive the pressure and the chemical potential.^{2,40} The chemical potential is given by

$$\vartheta(\mathbf{x}) := \frac{\delta \mathcal{F}}{\delta \phi} = \frac{3\gamma}{\sqrt{8\ell}} (\phi^3 - \phi - \ell^2 \nabla^2 \phi) - \frac{1}{2} (\partial_\phi \varepsilon) \mathbf{D} \cdot \mathbf{E}, \quad (9)$$

where the symbol $\delta/\delta\phi$ denotes the functional derivative with respect to the function ϕ . In consequence, the stresses derived from the free energy are given by,^{41,42}

$$\mathbf{\Pi}(\mathbf{x}) = (\phi\vartheta - \psi)\mathbf{I} + \frac{3\gamma\ell}{\sqrt{8}}\nabla\phi\nabla\phi^T - \mathbf{D}\mathbf{E}^T, \quad (10)$$

where \mathbf{I} corresponds to the identity matrix, T denotes matrix transposition. Eq. (10) can be split in two: the thermodynamic and electric contributions, namely, $\mathbf{\Pi} = \mathbf{P} - \mathbf{T}$. The first one, \mathbf{P} , is the pressure tensor from Eq. (2) such that its divergence results in the capillary forces in the diffuse interface formalism, to be precise, $-\nabla \cdot \mathbf{P} = -\phi\nabla\vartheta = \mathbf{f}_{\text{cap}} - \nabla p$, where p corresponds to the hydrodynamic pressure; and the second one, \mathbf{T} , corresponds to the Maxwell stress tensor in the absence of magnetic fields,

$$\mathbf{T} := \mathbf{D}\mathbf{E}^T - \frac{1}{2}(\mathbf{D} \cdot \mathbf{E})\mathbf{I}. \quad (11)$$

The free charges, ρ_{el} , are derived from the energy functional,

$$\rho_{\text{el}}(\mathbf{x}) := -\frac{\delta\mathcal{F}}{\delta V} = \nabla \cdot \mathbf{D}, \quad (12)$$

which we identify as Gauss's law for continuous dielectric media.² Then, in the absence of free charges and homogeneous electric permittivity, Eq. (12) reduces to Laplace's equation for the electric potential, $\nabla^2 V = 0$.

Equivalently, and for simplicity, the electrostatic stresses can be turned into a body force,^{2,25,26}

$$\mathbf{f}_{\text{el}} := \nabla \cdot \mathbf{T} = \rho_{\text{el}}\mathbf{E} - \frac{1}{2}|\mathbf{E}|^2\nabla\varepsilon. \quad (13)$$

From the first term of the right-hand side of Eq. (13), we recognise the Lorentz force due to the electrostatic field on the free charges; the following term corresponds to the polarisation forces that emerge due to changes in the permittivity of the medium. For neutrally charged dielectrics, the free charge density is zero, thus vanishing the first term of the force. For

incompressible fluids, $\nabla\varepsilon$ is zero everywhere except in the neighbourhood of an interface, therefore, the force points in the perpendicular direction to the interface from the dielectric of higher permittivity to lower permittivity.

There are alternative models for the dielectrophoretic force derived from the interaction of molecular or atomic dipoles that constitute the dielectric media in response to an external field. The force exerted on a dipole is given by $(\mathbf{p} \cdot \nabla)\mathbf{E}$, where \mathbf{p} is the dipole moment.¹ Additionally, the strength of dipole is proportional to the electric field, $\mathbf{p} \propto \mathbf{E}$. This results in a force that is proportional to gradients in the electric field,^{4,15,43} i.e., $\mathbf{f}'_{\text{el}} = (\varepsilon - \varepsilon_0)\nabla|\mathbf{E}|^2/2$. This model of the dielectrophoretic forces implies that a non-zero force is found in the bulk of dielectric media whenever gradients in the magnitude of the electric field are present. In contrast, the expression in Eq. (13) shows that the forces are localised at the interface between media of different permittivity. However, this is only an apparent contradiction since the two forcing models differ by the gradient of the electric energy density, that is, $\mathbf{f}_{\text{el}} = \mathbf{f}'_{\text{el}} - \nabla[(\varepsilon - \varepsilon_0)|\mathbf{E}|^2]/2$. Therefore, when employing the dielectrophoretic forces, \mathbf{f}'_{el} , the hydrodynamic pressure is shifted by an amount $p' = p + (\varepsilon - \varepsilon_0)|\mathbf{E}|^2/2$. This additional term cancels \mathbf{f}'_{el} by means of $-\nabla p'$ in the bulk of a phase where ε is constant, therefore, eliminating the body forces absent in Eq. (13). Note that this additional term in p' is required for mechanical equilibrium; otherwise, in the presence of a net body force, the fluid would not be able to settle at rest.

We specify the boundary conditions for the coupled set of PDEs, equations (2), (3) and (12) for all boundary points $\mathbf{x}_b \in \partial\Omega$. To impose the impenetrability and no-slip boundary condition at solid boundaries we write,

$$\mathbf{u}(\mathbf{x}_b) = 0, \tag{14}$$

for the velocity field, and to enforce the wetting behaviour of the fluid-fluid mixture we set

$$\hat{\mathbf{n}} \cdot \nabla \phi(\mathbf{x}_b) = -\frac{\sqrt{8}}{3\gamma\ell} \zeta(\theta_e), \quad (15)$$

for the phase field, where $\hat{\mathbf{n}}$ is the unit normal to the solid boundary. Regardless of the no-slip boundary condition, the mobility of the contact lines^{44,45} occurs by the diffusion of the chemical potential given by Eq. (3). For ideally smooth surfaces, the boundary value of the right-hand side of Eq. (15) can be set to a constant, however, this seldomly occurs in real surfaces that present inhomogeneities down to a microscopic level.⁴⁶ Therefore, surface roughness can be introduced by altering the geometry of the surface, or by introducing a noisy component to the wetting potential.⁴⁷

We specify two types of boundary conditions for the electric field. If the electric field at the solid boundary is specified by an electrode on the surface, then we impose

$$V(\mathbf{x}_b) = V_b \quad (16)$$

if the field is specified by polarisation charges, then

$$\hat{\mathbf{n}} \cdot \nabla V(\mathbf{x}_b) = -\frac{\sigma_b}{\varepsilon - \varepsilon_s}, \quad (17)$$

where σ_b corresponds to the bound surface charge density and ε_s is the permittivity of the solid.

The Lattice Boltzmann Algorithm

The lattice-Boltzmann method simulates the dynamics of fluids by numerically integrating the Boltzmann equation from Kinetic Theory. This is based on the statistical description of the fluid by introducing a distribution function, $f_q(\mathbf{x}, t)$, that corresponds to the mean

density of particles that are found in a discrete position \mathbf{x} , with velocity \mathbf{c}_q and at time t .

The lattice-Boltzmann algorithm consists of two steps. The streaming of the distribution function,

$$f_q(\mathbf{x} + \mathbf{c}_q, t + 1) = f_q^*(\mathbf{x}, t), \quad (18)$$

followed by the collision step, where we define the post-collision distribution function as

$$f_q^*(\mathbf{x}, t) := f_q(\mathbf{x}, t) + \mathcal{C}[f]_q + S_q. \quad (19)$$

During the streaming step, the particle populations migrate into neighbouring lattice positions given by the vector \mathbf{c}_q over a unitary time step ($\mathbf{x} \rightarrow \mathbf{x} + \mathbf{c}_q$). Therefore, the velocities $\mathbf{c}_q \in \{\mathbf{c}_q\}_{q=0}^{Q-1}$ are a set of Q , D -dimensional vectors of integer entries that specify the connectivity of the lattice. Conventionally, this is summarised by the D - Q - notation for the lattice-Boltzmann model, in our case we use the models $D2Q9$ and $D3Q15$, meaning $D = 2, 3$ with $Q = 9, 15$, respectively. During the collision step in Eq. (19), the second term of the right-hand side corresponds to the collision operator, $\mathcal{C}[f]_q$, and the sources term, S_q , respectively.

The source term in Eq. (19) can take multiple forms, depending on the type of sources to include in the evolution of the distribution function, for example, sources of mass, forces, or stresses. These will be specified in the following subsections.

In the collision operator, we adopt a linear multiple-relaxation time (MRT) scheme.⁴⁸ While there are several ways to implement the MRT algorithm,^{29,49} all agree on the relaxation of the distribution function towards some local equilibrium, f_q^e , for which there are different relaxation rates for each component of the distribution function. This is usually done by carrying out a transformation from the space of distribution functions, $f = \{f_q\}_{q=0}^{Q-1}$, into a space of moments, $m = \{m_i\}_{i=0}^{\infty}$, such that $\mathcal{T}[f] = m$, and inverse transform $\mathcal{T}^{-1}[m] = f$. Since the moments of the distribution function bear physical significance, this allows to selectively tune the viscosity, thermal conductance and other transport coefficients independently

by means of the relaxation rates,⁵⁰ ω_i ,

$$\mathcal{C}[f] := \mathcal{T}^{-1} [\{-\omega_i(m_i - m_i^e)\}], \quad (20)$$

where the $m^e := \mathcal{T}[f^e]$ are the moments of the local equilibrium.

The approach we adopt here is to employ the multidimensional discrete Hermite transform

$$m_i(\mathbf{x}, t) = \mathcal{T}[f]_i := \sum_{q=0}^{Q-1} H_i(\mathbf{c}_q/c_s) f_q(\mathbf{x}, t) \quad (21)$$

where H_i denotes the i -th Hermite tensor polynomial, eg., $H_0(\boldsymbol{\xi}) = 1$, $H_1(\boldsymbol{\xi}) = \boldsymbol{\xi}$, $H_2(\boldsymbol{\xi}) = \boldsymbol{\xi}\boldsymbol{\xi}^T - \mathbf{I}$, and so on; and the inverse of the discrete Hermite transform,

$$f_q(\mathbf{x}, t) = \mathcal{T}^{-1}[m]_q := \sum_{i=0}^{\infty} \frac{w_q}{i!} H_i(\mathbf{c}_q/c_s) \odot m_i(\mathbf{x}, t). \quad (22)$$

In contrast with its continuous counterpart, the discrete Hermite transform replaces the integration by a sum of the index q . However, the direct and inverse discrete Hermite transform can be done without loss in precision by using the Gauss-Hermite quadrature rule.⁵¹ This gives value to the speed of sound, c_s , and the weights, w_q .

We note here that, for Eq. (22) to be an inverse, it must be a one-to-one mapping, and therefore, only Q elements in all the moments m_i are independent. The moment m_i inherits the rank of the tensor H_i , e.g., m_0 is a scalar, m_1 is a vector, and so on. It is implied that the symbol \odot in Eq. (22) is a generalisation of the dot product, which contracts two tensors of the same rank into a scalar, e.g., vector dot product for $i = 1$ and the trace of the matrix product or double dot product for $i = 2$.

For the boundary conditions, we follow Ginzburg⁵² in which two types of boundary conditions are discussed: *bounceback*⁵³ and *antibounceback*. The bounceback algorithm is employed to specify a Dirichlet boundary condition for the moment m_1 . Since m_1 is a vector, it is often used to prescribe the velocity of the fluid or diffusive flows at the boundary. The

antibounceback algorithm is used to prescribe a Dirichlet boundary condition on the moments m_0 and m_2 . The zeroth and second moments of a distribution function are related to the density, the hydrodynamic pressure and other stresses that act on the fluid. Therefore, this boundary condition is often used to prescribe open boundaries that allow inward or outward fluxes to the simulation domain.

The lattice-Boltzmann method has proven to be effective in solving the evolution equations even for systems beyond fluid dynamics. This is due to the underlying mathematical structure of the algorithm which is revealed by the Chapman-Enskog analysis^{32,54} (see Supporting Information I). In conclusion, one can reconstruct a broad range of dynamical equations by tuning the components of Eq. (19). We exploit this virtue to numerically integrate the Navier-Stokes and Cahn-Hilliard equations for the dynamics of the fluid, and also to find the electric field, in accordance with Gauss's law.

In the following, we will use Eqs. (18) through (22) as stencils for the different equations in which we apply the lattice Boltzmann algorithm.

Integrating the Navier-Stokes equation

We begin by applying the LBM to solve the Navier-Stokes equation (2). To avoid confusion in the following subsections, we have used the subscript f in m_{fi} and ω_{fi} to specify the i -th moment and collision parameter that correspond to the f_q distribution. The first moments of the distribution function define macroscopic variables,

$$\rho := m_{f0} = \sum_{q=0}^{Q-1} f_q, \quad (23)$$

for the mass density and

$$\rho \mathbf{u} := m_{f1} c_s = \sum_{q=0}^{Q-1} \mathbf{c}_q f_q, \quad (24)$$

for the momentum density. The equilibrium distribution function constructed by discretising the Maxwell-Boltzmann distribution, in other words, by setting, $m_{f0}^e := \rho$, $m_{f1}^e := \rho \mathbf{u} / c_s$,

and $m_{f_2}^e := \rho \mathbf{u} \mathbf{u}^T / c_s^2$ using Eq. (22), this results in the common expression,²⁹

$$f_q^e(\rho, \mathbf{u}) := \rho w_q \left[1 + \frac{\mathbf{u} \cdot \mathbf{c}_q}{c_s^2} + \frac{1}{2} \left(\frac{\mathbf{u} \cdot \mathbf{c}_q}{c_s^2} \right)^2 - \frac{|\mathbf{u}|^2}{2c_s^2} \right]. \quad (25)$$

Following a Chapman-Enskog analysis (see Supporting Information I), the constant ω_{f_2} in the collision operator, prescribes the value for the dynamic viscosity, μ , thus we set

$$\omega_{f_i} = \begin{cases} 1 & \text{if } i \neq 2 \\ \frac{2}{1+2\mu/\rho c_s^2} & \text{if } i = 2 \end{cases}. \quad (26)$$

To implement the coupling of the capillary and electric forces we specify the sources term, $S_q = S_q^{(\text{cap})} + S_q^{(\text{el})}$ in the post-collision distribution. The capillary forces are included from the pressure tensor defined in Eq. (10),

$$S_q^{(\text{cap})} = \frac{w_q}{2c_s^2} H_2(\mathbf{c}_q/c_s) : \mathbf{P}, \quad (27)$$

where the symbol $:$ corresponds to the double-dot product. We do not include the Maxwell's stress tensor in Eq. (27) due the convenience that the simple expression in Eq. (13) gives. In turn, we add the electric forces following Guo's et al.⁵⁵ forcing scheme,

$$S_q^{(\text{el})} = \frac{w_q}{c_s^2} \left[(\mathbf{c}_q - \mathbf{u}) + \frac{(\mathbf{u} \cdot \mathbf{c}_q)}{c_s^2} \mathbf{c}_q \right] \cdot \mathbf{f}_{\text{el}}. \quad (28)$$

We prescribe the solid and closed boundaries using an interpolated bounceback as in Yu *et al.* (2003).⁵³ In this way, we can specify impenetrability and no-slip boundary conditions on walls. For open walls, we follow Ginzburg *et al.* (2)⁵² antibounceback to prescribe the pressure and density of the fluid at the boundary.

Integrating the Cahn-Hilliard equation

The Cahn-Hilliard equation (3) belongs to a family of convection-diffusion equation and can be solved by the lattice-Boltzmann formalism as well. We follow the scheme developed by Swift et al.^{32,54} using another distribution function, g_q , which is solved by a new lattice-Boltzmann equation, (18) and (19). We now refer to m_{gi} and ω_{gi} as the moments and collision parameters that correspond to the distribution g_q .

The zeroth moment of the distribution gives value to the phase field,

$$\phi := m_{g0} = \sum_{q=0}^{Q-1} g_q. \quad (29)$$

The equilibrium distribution, g_q^e , is constructed such that the phase field is advected by the flow field \mathbf{u} and diffused by the chemical potential, μ , as defined in Eq. (9),

$$g_q^e(\phi, \mathbf{u}, \mu) = \phi \delta_{q0} + 2w_q M \mu / c_s^2 + \phi w_q \left[\frac{\mathbf{u} \cdot \mathbf{c}_q}{c_s^2} + \frac{1}{2} \left(\frac{\mathbf{u} \cdot \mathbf{c}_q}{c_s^2} \right)^2 - \frac{|\mathbf{u}|^2}{2c_s^2} \right], \quad (30)$$

where δ_{qr} is the Kronecker symbol (if $r = q$, returns 1 and 0 otherwise). Performing a Chapman-Enskog analysis, it can be shown that by setting the collision parameters to $\omega_{gi} = 1$ we recover the Cahn-Hilliard equation.

To calculate the chemical potential and pressure tensor, the gradient and Laplacian operators of the phase field are required. We use the finite differences stencil defined by Pooley *et al.* (2008)⁵⁶ to increase the accuracy and stability of the numerical method.

The boundary conditions specified for the g_q distribution function are similar to f_q : we use an interpolated bounceback to specify impenetrability and no-slip boundary conditions, and antibounceback to specify the phase field and chemical potential at the boundaries.

Calculating the Electric Field

Among the equations that govern the dynamics of the system, Gauss's law (12) is independent of time. As opposed to the complete set of Maxwell's equations, we are not interested in the dynamics of the electromagnetic fields, since the velocities expected from capillary phenomena are several orders of magnitude smaller than the speed of light.⁵⁷ Therefore, we assume that the potential relaxes instantaneously. For that reason, our strategy is to use a relaxation method at every time step to find the electric field, and this will be provided within the framework of the lattice-Boltzmann method. We use a third distribution function, h_q , and lattice-Boltzmann equation iteratively, and corresponding m_{hi} and ω_{hi} for the moments and collision parameters, respectively. Then, based on Eqs. (18) and (19), we replace the time variable with an iteration counter, t' , to have,

$$h_q(\mathbf{x} + \mathbf{c}_q, t' + 1) = h_q^*(\mathbf{x}, t'), \quad (31)$$

and from which, we proceed to define the post-collision distribution, h_q^* .

We define the zeroth moment of the distribution function by a mock variable, \tilde{V} , which converges to the electric potential, i.e., $\lim_{t' \rightarrow \infty} \tilde{V}(\mathbf{x}, t') = V(\mathbf{x})$, then,

$$\tilde{V}(\mathbf{x}, t') := m_{h0} = \sum_{q=0}^{Q-1} h_q(\mathbf{x}, t'). \quad (32)$$

The equilibrium distribution is built from $m_{h0}^e := \tilde{V}$, and $m_{hi}^e := 0$ for $i > 0$, which results in the expression,

$$h_q^e := w_q \tilde{V}. \quad (33)$$

The electric permittivity plays the role of the diffusion constant in Gauss's law. Therefore,

we can prescribe the value of the electric permittivity through the collision parameters,

$$\omega_{hi} = \begin{cases} 1 & \text{if } i \neq 1 \\ \frac{2}{1+2\varepsilon} & \text{if } i = 1 \end{cases}. \quad (34)$$

In this way, the equation of motion for \tilde{V} is derived from the zeroth moment of the collision operator, $-\omega_{h0}(m_{h0} - m_{h0}^e) \equiv 0$ (see Supporting Information I),

$$c_s^2 \nabla \cdot (\varepsilon \nabla \tilde{V}) - \partial_{t'} \tilde{V} + \frac{1}{2} \partial_{t'}^2 \tilde{V} = 0, \quad (35)$$

where t' is now reinterpreted as a continuous variable. From the evolution of the first moment of the collision operator (see Supporting Information I) we define,

$$\tilde{\mathbf{E}} := \frac{2(m_{h1} - m_{h1}^e)}{c_s(\varepsilon + 1)} = -\nabla \tilde{V} + 2(1 + 2\varepsilon) \nabla \partial_{t'} \tilde{V} \quad (36)$$

which, similarly, converges to the electric field as the term $\partial_{t'} \tilde{V}$ vanishes, i.e., $\lim_{t' \rightarrow \infty} \tilde{\mathbf{E}} = \mathbf{E}$. This implies that, once h_q has relaxed to the steady state, it is no longer necessary to compute the electric field via a finite differences scheme.

In summary, in the limit $t' \rightarrow \infty$, the moments of the distribution function converge to,

$$V = \sum_{q=0}^{Q-1} h_q, \quad \text{and} \quad \mathbf{E} = \frac{2c_s^{-2}}{\varepsilon + 1} \sum_{q=0}^{Q-1} \mathbf{c}_q h_q. \quad (37)$$

Therefore, post-collision distribution in Eq. (31) reduces to,

$$h_q^*(\varepsilon, V, \mathbf{E}) := w_q \left[V + \frac{1}{2} (\varepsilon - 1) \mathbf{c}_q \cdot \mathbf{E} \right], \quad (38)$$

which can be substituted into Eq. (31) simplifying the collision and streaming steps. We emphasise that both the electric potential, V , and electric field, \mathbf{E} , are being calculated by the algorithm, therefore, exempting the need to calculate explicitly the electric field from

the gradient of the potential with yet another method. This is particularly convenient since it ensures consistency concerning the boundary conditions.

The boundary conditions are specified in the spirit of the LBM formalism.⁵² During the streaming step, the particle populations are gathered from the neighbouring nodes, this implies that for nodes near a boundary some populations of particles representing with velocity in opposite direction to the boundary are absent. The boundary conditions are prescribed by reconstructing the missing particle populations. To be precise, let us define \mathbf{x}_{nb} as a near-boundary lattice node such that a displacement $\alpha_q \mathbf{c}_q$, $0 < \alpha_q \leq 1$, reaches a point on the boundary, i.e., $\mathbf{x}_{\text{nb}} + \alpha_q \mathbf{c}_q \in \partial\Omega$. Then, let us define \bar{q} as the index with direction opposite to the boundary, i.e., $\mathbf{c}_{\bar{q}} + \mathbf{c}_q = 0$. By employing a linear interpolated antibounceback scheme, we are able to prescribe Dirichlet boundary conditions for the electric potential (Eq. (16)), V_b ,

$$h_{\bar{q}}(\mathbf{x}_{\text{nb}}, t' + 1) = w_q V_b + \left(\frac{1}{2} - \alpha_q \right) h_q^*(\mathbf{x}_{\text{nb}}, t') + (\alpha_q - 1) h_q^*(\mathbf{x}_{\text{nb}} - \mathbf{c}_q, t') + \frac{1}{2} h_{\bar{q}}^*(\mathbf{x}_{\text{nb}}, t'), \quad (39)$$

and utilising a linear interpolated bounceback⁵³ prescribes Neumann boundary conditions, in the absence of boundary charges (Eq. (17)), this becomes

$$h_{\bar{q}}(\mathbf{x}_{\text{nb}}, t' + 1) = \frac{\alpha_q}{1 + \alpha_q} (h_q^*(\mathbf{x}_{\text{nb}}, t') + h_{\bar{q}}^*(\mathbf{x}_{\text{nb}}, t')) + \frac{1 - \alpha_q}{1 + \alpha_q} h_q^*(\mathbf{x}_{\text{nb}} - \mathbf{c}_q, t'). \quad (40)$$

Higher-order approximations and other boundary conditions are available in the lattice-Boltzmann formalism.²⁹

Results and discussion

Assessment of the numerical method

First, we assess the validity of the numerical method. To do this, we perform two basic tests against exact solutions to Gauss's equation of two configurations. For both systems, we can calculate the relative error of the numerical method against the analytic solution using the standard deviation formula,

$$\text{Err}(t') := \left[\frac{1}{|\Omega|} \sum_{\mathbf{x}}^{\Omega} \left(\tilde{V}(\mathbf{x}, t') - V(\mathbf{x}) \right)^2 \right]^{1/2}. \quad (41)$$

As a relaxation method, the error decreases exponentially with the number of iterations, which can be verified from Eq. (35) (see Supporting Information II for details). We estimate the worst-case scenario for the number of iterations that characterise the exponential relaxation by

$$\tau_V(\varepsilon) = \left[\left(1 + 2\varepsilon \frac{c_s^2 \pi^2}{L^2} \right)^{1/2} - 1 \right]^{-1}, \quad (42)$$

where $L = \max\{L_x, L_y, L_z\}$, is the greatest of the sides of the simulation domain.

In the first test, the configuration consists of an array of interdigitated electrodes in free space of periodicity λ and vanishing thickness. The simulation consists of a D2Q9 lattice-Boltzmann. The domain of the simulation consists of a simulation rectangle of sides L_x , and $L_y = L_x + 1$ with periodic boundary conditions at $x = 0$ and $x = \lambda = L_x$ and Dirichlet boundary conditions at $y = \pm[L_y/2]$, where the boundary value is given by evaluating the analytical solution (see Supporting Information III for the expression). The electric potential at the electrodes is prescribed by overriding the value of \tilde{V} at the location of the electrodes

and using Eq. (32) elsewhere, that is,

$$\tilde{V}(\mathbf{x}) = \begin{cases} \frac{1}{2}V_b \operatorname{sgn}[\sin(2\pi x/Lx)] & \\ \text{if } z = 0 \text{ and } |\cos(\pi s/2)| > |\sin(2\pi x/\lambda)| & \\ \sum_{q=0}^{Q-1} h_q & \text{otherwise} \end{cases} \quad (43)$$

for all t' , where s is the fraction of area covered by the electrodes, that is, the electrode width-to-periodicity ratio. Eq. (43) prescribes a constant value in the electric potential implying these are the conductors, whereas everywhere else is subject to Laplace's equation.³³

In Fig. 1a we present the resulting electric potential obtained by the lattice-Boltzmann algorithm. Fig. 1b shows a comparison of the numerical method against the exact solution for varying s showing good agreement. Then, we quantify the error of the numerical algorithm and show that it decreases exponentially with the number of iterations (see Fig. 1c). It can be observed that the error decreases exponentially at a steady pace, but eventually reaches a stagnation state where, for a given value of L_x , the algorithm cannot improve the accuracy. This can be attributed to the resolution of the numerical algorithm since it assigns a lattice site for the thickness of the electrodes in contrast to the exact solution which is zero. Therefore, by increasing the domain size, the thickness of the electrodes relative to the simulation size is reduced, and consequently, the error (see Fig. 1d).

The second test consists of a two-dielectric, parallel plate capacitor. On one end of the simulation domain ($x = 0$) the electric potential is set to $V = -V_b/2$, while on the opposite end ($x = L_x - 1$) it is set to $V = V_b/2$, thus making a potential difference of V_b . The domain is filled with two different dielectric permittivities, ε_1 and ε_2 filling the first and second half of the domain, respectively (see Fig. 2a). The exact solution for the electric potential of this

system is given by,

$$V(x) = \frac{V_b}{2(\varepsilon_1 + \varepsilon_2)L_x} \begin{cases} 4\varepsilon_2x - (\varepsilon_2 + \varepsilon_1)L_x & \text{if } 0 \leq x < \frac{L_x}{2} \\ 4\varepsilon_1x + (\varepsilon_2 - 3\varepsilon_1)L_x & \text{if } \frac{L_x}{2} < x \leq L_x \end{cases}. \quad (44)$$

The results of the relative error and convergence rate are reported in Fig. 2b and c as a function of the permittivity ratio between the two dielectrics. These are a set of simulations running for a total of $t' \leq 10\tau_V(\sqrt{\varepsilon_1\varepsilon_2})$ iterations, where $\tau_V \approx 2 \times 10^4$ is given in Eq. (42) evaluated at the geometrical mean of the two dielectric permittivities and simulation size $L_x = 256$. As can be observed from the figure, the error is kept at low values for permittivity ratios of 10^0 to 2×10^2 offering good convergence. The transient number of iterations is calculated by a simple linear regression on $\log \text{Err}(t')$ over the of iterations, t' . The inverse of the slope is plotted in Fig. 2(b). It can be observed the rise of the transient as the permittivity ratio increases, which according to Eq. (42), it is expected as ε_2 is decreased. After reaching a peak around $\varepsilon_1/\varepsilon_2 \sim 2 \times 10^2$, the numerical method cannot improve the accuracy. However, this lies beyond the requirements of many real substances, e.g., the relative permittivity of water⁵⁸ at 0 °C is $\varepsilon = 87.91 \pm 0.2$ and, in the experiments by Brown *et al.* (2015),⁵⁹ the permittivity ratio is lower than 70.

Wrinkling of a liquid-air interface

We now validate the numerical method by comparing it to the experimental results of Brown *et al.* (2009)⁷ for L-DEP in a two-phase system without a contact line. In that work, the system consisted of a thin liquid film in air covering a periodic array of electrodes (Fig. 1) and acted as a voltage programmable liquid optical interface. The film has a greater permittivity than the fluid above it, and the electrodes are set to a voltage difference V_b . In consequence, the liquid-air interface wrinkles balancing the electric and capillary forces.^{17,60} For this, we carried out the D2Q9 lattice-Boltzmann simulations as described before, but now including

the coupled dynamics of the dielectric fluids. We set $L_x = 1536$ and $L_y = 257$. The multiphase fluid is placed at $z \geq 1$, with one phase of thickness h_0 and electric permittivity ε_1 underneath another dielectric fluid of permittivity ε_2 . This is done by setting the phase field

$$\phi(\mathbf{x}, t = 0) = \tanh \left[\frac{h_0 + 1 - z}{\sqrt{2}\ell} \right] \quad (45)$$

and using Eq. (7). The fluid mixture is initialised at rest ($\mathbf{u}(\mathbf{x}, t = 0) = 0$), specified by the physical properties provided in Table 1 and is allowed to relax to mechanical equilibrium for a time $t = 3 \times 10^6$ in simulation units.

Fig. 3 shows the simulation results and a comparison against the experiments by Brown *et al.* (2009).⁷ The electric forces focus on the interface pushing it upwards. The magnitude of the force varies along the interface causing a distortion (see Fig. 3a, parameters chosen for clarity). Then, in Fig. 3b, it can be observed that the amplitude of the distortion of the interface increases with the electric potential. The profile of the liquid-air interface shows good agreement with the experimental observations. By expressing the interface profile, $h(x)$, in a Fourier cosine series,⁴³

$$h(x) = \sum_{n=0}^{\infty} \beta_n \cos(2\pi n x / \lambda), \quad (46)$$

we are able to compare in more detail the first coefficients of the series of the simulations against the experimental observations (see Fig. 3c) and remark the good agreement between the two.

Table 1: Simulation parameters (arbitrary units).

Parameter	Value	Parameter	Value
Surface tension, γ	5×10^{-3}	Interface thickness, ℓ	1.6
Density, ρ	1	Viscosity, η	8.3×10^{-3}
Mobility, M	2.4	Electrode width, s	1/2

Dielectrowetting of a droplet

We now validate the numerical method against a system with a dielectric liquid droplet immersed in a surrounding fluid (liquid or gas) on a solid surface, therefore having a three-phase contact line. As McHale *et al.* (2011)¹² described, the wetting of a surface is induced by the fringe field localised to the solid-fluid interface due to an array of interdigitated electrodes (see Fig. 4a, b). A conventional way of measuring the spreading of a droplet is by the contact angle. In the absence of electrostatic fields, the balance of forces gives the well known Young-Dupré relation⁶¹ (see Fig. 4c),

$$\gamma \cos \theta_e = \gamma_{sm} - \gamma_{sd}, \quad (47)$$

where θ_e is the equilibrium contact angle, and γ_{sm} and γ_{sd} are the surface tensions of the solid surface in contact with the surrounding medium and the droplet, respectively. When an electric field is present, the work done per unit area as the droplet replaces the medium that surrounds it is

$$\Delta w = \frac{\Delta \varepsilon V_b^2}{2\delta}, \quad (48)$$

where $\Delta \varepsilon = \varepsilon_d - \varepsilon_m$, is the electric permittivity difference, V_b is the voltage difference, and δ is called the penetration depth.⁶⁰ Including the contribution of the electrostatic energy to the Young-Dupré relation gives,

$$\cos \theta(V_b) = \cos \theta_e + \frac{\Delta \varepsilon V_b^2}{2\gamma\delta}, \quad (49)$$

which is known as the dielectrowetting equation.¹²

We carried out three-dimensional simulations of a cylindrical droplet representing a slice of a dielectrowetting droplet over one period of the electrode array. As before, we specify periodic boundary conditions on $x = 0$ and $x = L_x = \lambda = 32$ and close boundaries for every other direction to ensure the conservation of each of the fluid phases. The droplet

can spread along the y direction, which is longitudinal to the electrodes, with an overall length, $L_y = 300$. The solid surface is located at $z = 1/2$, where we employ Eq. (8) to prescribe the equilibrium contact angle. The electric potential is prescribed using Eq. (23) of the Supporting Information III where the potential difference between the electrodes is V_b . Although this is slightly different from the experiments, due to computational limitations of a finite domain, this gives a more accurate boundary condition.

As we are interested in the static states of dielectrowetting, we produce quasistatic simulations for the spreading of the droplet by slowly increasing V_b and allowing a time τ_M for mechanical relaxation. The increase in V_b is done to reach a final voltage V_f in 100 equal size steps, where V_f is such that $\Delta\varepsilon V_f^2/2\gamma\lambda = 1.5$. The time for mechanical relaxation during each step is $\tau_M = 6000$ in simulation units.

We begin by comparing the simulations against the dielectrowetting equation, Eq. (49). In its form, the penetration depth, δ , is the mean distance from the electrodes where the electric field is concentrated. This distance is estimated to scale with the size of the wavelength of the electrodes, λ , thus we assume

$$\delta = \frac{\lambda}{\Phi}. \quad (50)$$

Here, the Φ is a function ($\Phi = \Phi(s, \varepsilon_d, \varepsilon_m, \dots)$) that takes into account the factors that distort the electric field as it invades the dielectric, for example, the electrode width, s , the electric permittivities of the media, etc. Then, the dielectrowetting equation becomes

$$\cos\theta(V_b) = \cos\theta_e + \Phi \frac{\Delta\varepsilon V_b^2}{2\gamma\lambda}, \quad (51)$$

where V_b is the potential difference at the electrodes. Except for Φ , all the factors in the last term of Eq. (51) are known *a priori*, in this form of the equation, we can quantify Φ , and therefore, the penetration depth.

From the simulations, we observe that during the spreading of the droplet, the central part of the droplet is mostly circular. Therefore, in the same fashion of experiments (for

droplets of size significantly less than the capillary length⁶¹), we define the apparent contact angle by extrapolating the circular arc until it intersects the solid surface (see Fig. 5a). However, it can be observed that the shape of the droplet departs from a circular arc by bending more abruptly in the vicinity of the contact lines. We measure the deviation of the circular arc and the position of the true contact line by Δl .

Fig. 5b shows the simulation results together with the experimental results by McHale *et al.* (2011)¹² of the change in the apparent contact angle as a function of the potential difference with good agreement between the two. It can also be observed the linear increase in $\cos \theta$ with respect to V_b^2 at low values and a smooth change to a constant behaviour at high values. This is also correlated with the growth of Δl . In the plot, Δl is scaled with respect to λ , since the bending of the interface occurs over a distance $\delta \propto \lambda$ from the plane of the electrodes. It can be seen that, although the deviation is smaller than λ , for $\Delta \varepsilon V_b^2 / 2\gamma\lambda \leq 0.7$, but diverges at higher values and the droplet flattens into a liquid film of finite thickness. Due to conservation of volume, this is an incomplete spreading at an apparently zero contact angle. Whilst this seems paradoxical, it can be observed that in a closer look at the contact line, the interface approaches the solid surface at an angle closer to θ_e consistent with previous observations.^{8,15,62} In conclusion, the circular arc misrepresents the shape of the droplet at a high potential difference.

The distribution of the dielectrophoretic force is displayed in Fig. 5c, being most intense near the solid surface and vanishingly small away from the solid surface, where the electric field dies out. Moreover, the profile of the force also reveals that the dielectric force is most intense at the edges and gaps between the electrodes but weak at their centres. Since the force is not evenly distributed along the interface, the result is a subtle wrinkling of the contact line as observed in the experiments⁵⁹ (see Fig. 5d).

We emphasise that the asymptotic approach to a zero contact angle is *not* the saturation effect observed in Electrowetting,¹⁴ but caused by the dielectrophoretic force that repels the top section of the droplet, thus restricting the spreading.

Next, we vary the equilibrium contact angle, θ_e . To optimise the simulations to accommodate the droplet such that the initial and final states do not reach the boundaries of the simulation domain, we change L_z according to θ_e . This is done such that the free height of the droplet is $h_0 = 3L_z/4$ and $L_z = \lceil 54(1 - \cos \theta_e) / \sqrt{\theta_e - \cos \theta_e \sin \theta_e} \rceil$.

In Fig. 6a, a very consistent progression with respect to the predicted apparent contact angle, θ , can be observed. This occurs at low voltages, where the circular cap fit gives a good representation of the shape of the droplet. At high V_b , the deviation is increasingly large, emphasising the discrepancy between the circular cap and the shape of the droplet. We can observe the collapse into a master curve (see inset of Fig. 6). Therefore, to a good level of accuracy, this implies the existence of a universal curve for the apparent contact angle, to which, the equilibrium contact angle belongs.

Fig. 6b shows the change in the microscopic contact angle, θ_m , as a function of the potential difference. In the diffuse interface approximation, the shape of the interface in the vicinity of the contact line is blurry, therefore, we measure θ_m by extrapolating the contour surface $\phi = 0$, then calculating the unit-normal vector of the interface, $\hat{\mathbf{n}}$, at the surface. θ_m is calculated after averaging, for a wavelength λ ,³⁹ the normal angle of the fluid-fluid and the solid-fluid interfaces. As it can be observed the microscopic contact angle deviates by a small quantity with respect to the prescribed contact angle, i.e., $\theta_m \approx \theta_e$. This behaviour is expected since the microscopic contact angle is determined over a region of the order of the interface width, ℓ , from the solid surface. Compared to the capillary energy, the electrostatic energy has a much lower density since it scales inversely proportional to the penetration depth, δ . Therefore, in more realistic scenarios where $\ell/\delta \sim 10^{-6}$, the effect of the electric field on the microscopic contact angle will be negligible. In conclusion, it would be valid to assume, in a sharp interface formulation, that the microscopic contact angle under dielectrowetting does not change.

We now consider the case where a dielectric liquid droplet is immersed in a second dielectric liquid rather than simply air. This allows us to investigate the effect of varying the

electric permittivity of the droplet with respect to the surrounding medium. We compare the simulation results with the experiments by Brown *et al.* (2015).⁵⁹ This set of experiments relate the height-to-length ratio of the droplet, h/l , with respect to V_b ,⁵⁹

$$\frac{h}{l}(V_b) = \frac{h_0}{l_0} - \Phi \frac{\Delta\varepsilon(V_b - C)^2}{4\gamma\lambda}, \quad (52)$$

where h_0 and l_0 are the height and length of the droplet in the absence of electric fields, and C is an offset on the abscissa that will be used as a fitting parameter.

We divide the experiments into two subsets depending on the surrounding medium: air (Fig. 7a), and another dielectric liquid of lower permittivity than the droplet (Fig. 7b). In both cases, it can be observed the linear dependence at low values of V_b^2 and tailing off at high values which is in good agreement with the experiments. As opposed to droplets embedded in air where $C = 0$, when the droplet is surrounded by another liquid, the spreading presents contact line pinning. In this set of experiments, it can be observed that the spreading of the droplet begins at a non-zero voltage. Then, for a fair comparison to the simulations, we allow $C \neq 0$ and find its value via curve fitting. A good agreement with the experiments on the spreading can be observed in Fig. 7b.

In Fig. 7c we reproduce the simulations, however keeping the contact angle constant to isolate the effect of a varying electric permittivity. It can be observed that the slope, indicated by the function Φ in Eq. (50), has a weak dependence on the permittivity ratio $\varepsilon_r := \varepsilon_d/\varepsilon_m$ (see inset of Fig. 7c). According to Brown *et al.* (2015),⁵⁹ we expect this behaviour since the dielectrophoretic forces are stronger, not only by the difference in electric permittivity, $\Delta\varepsilon$, but also by an increase in the permittivity ratio which amplifies the discontinuity of the electric field as the droplet becomes thinner. An increase in Φ translates in the reduction of the penetration depth by virtue of Eq. (50). This implies that the dielectric force is localised in a smaller vicinity of the contact line and, as expressed by Eq. (49), gives an additional contribution to the spreading of the droplet.

Conclusions

We have presented a new method capable of simulating multiphase dielectric fluids coupled with electric fields. This new method is based on the lattice-Boltzmann algorithm to solve the electrostatic equations together with the hydrodynamic equations, thus eliminating the need for alternative methods to tackle the electrostatic part separately. The method is based on the diffuse interface formalism, which models the dynamics of the capillary system also eliminating the need of tracking the fluid-fluid interface. While the present method focuses on dielectrics, it can be complemented by the one proposed by Ruiz-Gutierrez and Ledesma-Aguilar (2019)³³ to include conducting media as well.

We have analysed the numerical method in terms of its accuracy and convergence for a wide range of electric permittivities which include most real liquids. We first validate these findings by comparing the numerical method against exact solutions of simple systems. Then we validate the method against representative experiments of liquid dielectrophoresis (L-DEP) with good agreement. These are the wrinkling of the liquid-air interface of a dielectric liquid film, and the spreading of a droplet in air or a second liquid by dielectrowetting. We have shown that a balance of the dielectrophoretic and the capillary forces are responsible for the shape of the interface, therefore, a good match in the shape of the fluids is a testament to the accuracy of the method as shown in the wrinkling of the interface of a dielectric film. We also validate the numerical method against dielectrowetting where we measure the spreading of a liquid by its contact angle and, equivalently, its height. With the capability of simulating dielectrowetting setups, further exploration of the dynamics of liquid fronts during spreading, and electrode design, for example, are now available. Beyond the experimental observations on dielectrowetting, we analysed the forces that produce the spreading of the droplet. We showed that these are stronger at the edges and gaps of the electrodes where the electric field is most intense and weaker at the centre of the electrodes. By analysing the shape of the droplet we investigate the effect of the electric field on the microscopic contact angle and showed that, up to numerical limitations, it remains invariant upon the presence of an

electric field. At high potential differences, the droplet gradually becomes a film. Therefore, the apparent contact angle, calculated by fitting a circular arc to the fluid-fluid interface, fails to measure the spreading of the droplet. Finally, under a close examination, by varying the permittivity contrast between the droplet and the surrounding medium, we observed that the penetration depth decreases with respect to the permittivity ratio, thus, contributing to the spreading of the droplet.

This numerical method is not restricted to dielectrowetting, and it opens the possibility of modelling and analysing electrocapillary systems that are still challenging to tackle. The algorithm proposed in this work to solve Gauss's law benefits from the framework of the lattice-Boltzmann method. These include optimisation for parallel execution and ease for implementing the boundary conditions where the voltage or the charges are prescribed at off-lattice sites. Although we have restricted this study to perfect dielectrics, more realistic media, e.g., leaky dielectrics or materials that present dielectric breakdown, can be included in the algorithm employing a source term in Eq. (38). In this way, the broad phenomena of electrocapillarity can be modelled efficiently within a single framework, this includes, for instance, falling films enhanced by electric fields and electrospinning techniques.

Acknowledgement

This work was supported by the U.K. Engineering and Physical Sciences Research Council grants EP/R042276/1 and EP/R036837/1.

Supporting Information Available

Details of the

1. Chapman-Enskog analysis of the lattice-Boltzmann equation
2. Convergence of the algorithm to the solution of Gauss's law

3. The Electric Potential of Interdigitated Electrodes

can be found in `suppinfo.pdf`

References

- (1) Jackson, J. D. *Classical electrodynamics*; Wiley, 1999.
- (2) Landau, L. D.; Bell, J. S.; Kearsley, M. J.; Pitaevskii, L. P.; Lifshitz, E. M.; Sykes, J. B. *Electrodynamics of continuous media*; Elsevier, 2013; Vol. 8.
- (3) Pohl, H. A. *Dielectrophoresis: The behavior of neutral matter in nonuniform electric fields*; Cambridge University Press, 1978.
- (4) Jones, T. B. *Electromechanics of Particles*; Cambridge University Press, 1995.
- (5) Jones, T. B. Liquid dielectrophoresis on the microscale. *J. Electrostat* **2001**, *51-52*, 290–299.
- (6) Hutchings, I. M.; Martin, G. D. *Inkjet technology for digital fabrication*; John Wiley & Sons, 2012.
- (7) Brown, C. V.; Wells, G. G.; Newton, M. I.; McHale, G. Voltage-programmable liquid optical interface. *Nat Photonics* **2009**, *3*, 403–405.
- (8) McHale, G.; Brown, C. V.; Newton, M. I.; Wells, G. G.; Sampara, N. Developing interface localized liquid dielectrophoresis for optical applications. *Optical Design and Testing V*. 2012; pp 13 – 20.
- (9) Gangwal, S.; Cayre, O. J.; Velev, O. D. Dielectrophoretic Assembly of Metallodielectric Janus Particles in AC Electric Fields. *Langmuir* **2008**, *24*.
- (10) Teo, W. E.; Ramakrishna, S. A review on electrospinning design and nanofibre assemblies. *Nanotechnology* **2006**, *17*, R89–R106.

- (11) Jones, T. B.; Fowler, J. D.; Chang, Y. S.; Kim, C.-J. Frequency-Based Relationship of Electrowetting and Dielectrophoretic Liquid Microactuation. *Langmuir* **2003**, *19*, 7646–7651.
- (12) McHale, G.; Brown, C. V.; Newton, M. I.; Wells, G. G.; Sampara, N. Dielectrowetting Driven Spreading of Droplets. *Phys Rev Lett* **2011**, *107*, 186101.
- (13) Jones, T. B. On the Relationship of Dielectrophoresis and Electrowetting. *Langmuir* **2002**, *18*, 4437–4443.
- (14) Mugele, F.; Heikenfeld, J. *Electrowetting: fundamental principles and practical applications*; John Wiley & Sons, 2018.
- (15) Russell, A. C.; Hsieh, W. L.; Chen, K. C.; Heikenfeld, J. Experimental and Numerical Insights into Isotropic Spreading and Deterministic Dewetting of Dielectrowetted Films. *Langmuir* **2015**, *31*, 637–642.
- (16) Wray, A. W.; Matar, O. K.; Papageorgiou, D. T. Accurate low-order modeling of electrified falling films at moderate Reynolds number. *Phys Rev Fluids* **2017**, *2*, 063701.
- (17) Chappell, D. J.; O’Dea, R. D. Numerical-asymptotic models for the manipulation of viscous films via dielectrophoresis. *J Fluid Mech* **2020**, *901*, A35.
- (18) Kaler, K. V. I. S.; Prakash, R.; Chugh, D. Liquid dielectrophoresis and surface microfluidics. *Biomicrofluidics* **2010**, *4*, 022805.
- (19) Geng, H.; Cho, S. K. Dielectrowetting for Digital Microfluidics: Principle and Application. A Critical Review. *Rev Adhes Adhes* **2017**, *5*, 268–302.
- (20) Edwards, A.; Brown, C.; Newton, M.; McHale, G. Dielectrowetting: The past, present and future. *Curr Opin Colloid Interface Sci* **2018**, *36*, 28 – 36.
- (21) Lin, Y.; Skjetne, P.; Carlson, A. A phase field model for multiphase electrohydrodynamic flow. *Int J Multiph Flow* **2012**, *45*, 1–11.

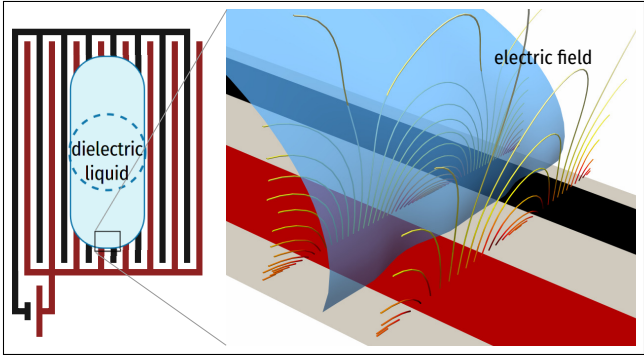
- (22) Gorthi, S. R.; Mondal, P. K.; Biswas, G.; Sahu, K. C. Electro-capillary filling in a microchannel under the influence of magnetic and electric fields. *Can J Chem Eng* **2021**, *99*, 725–741.
- (23) Pozrikidis, C. *A Practical Guide to Boundary Element Methods with the Software Library BEMLIB*; CRC Press, 2002.
- (24) Popinet, S. An accurate adaptive solver for surface-tension-driven interfacial flows. *J Comput Phys* **2009**, *228*, 5838–5866.
- (25) Tomar, G.; Gerlach, D.; Biswas, G.; Alleborn, N.; Sharma, A.; Durst, F.; Welch, S.; Delgado, A. Two-phase electrohydrodynamic simulations using a volume-of-fluid approach. *J Comput Phys* **2007**, *227*, 1267–1285.
- (26) Sahu, K. C.; Tripathi, M. K.; Chaudhari, J.; Chakraborty, S. Simulations of a weakly conducting droplet under the influence of an alternating electric field. *Electrophoresis* **2020**, *41*, 1953–1960.
- (27) Boyd, J. P. *Chebyshev and Fourier spectral methods*; Courier Corporation, 2001.
- (28) Canuto, C.; Hussaini, M.; Quarteroni, A.; Zang, T. *Spectral Methods: Evolution to Complex Geometries and Applications to Fluid Dynamics*; Springer Berlin Heidelberg, 2007.
- (29) Krüger, T.; Kusumaatmaja, H.; Kuzmin, A.; Shardt, O.; Silva, G.; Viggien, E. M. *The Lattice Boltzmann Method: Principles and Practice*; Springer, 2016.
- (30) Desplat, J. C.; Pagonabarraga, I.; Bladon, P. LUDWIG: A parallel Lattice-Boltzmann code for complex fluids. *Computer Physics Communications* **2001**, *134*, 273–290.
- (31) Latt, J. et al. Palabos: Parallel Lattice Boltzmann Solver. *Compu Math with Appl* **2021**, *81*, 334–350.

- (32) Swift, M. R.; Orlandini, E.; Osborn, W. R.; Yeomans, J. M. Lattice Boltzmann simulations of liquid-gas and binary fluid systems. *Phys Rev E* **1996**, *54*, 5041.
- (33) Ruiz-Gutiérrez, É.; Ledesma-Aguilar, R. Lattice-Boltzmann Simulations of Electrowetting Phenomena. *Langmuir* **2019**, *35*, 4849–4859.
- (34) Landau, L. D.; Lifshitz, E. M. *Fluid Mechanics*; Elsevier, 2013; Vol. 6.
- (35) Cahn, J. W.; Hilliard, J. E. Free energy of a nonuniform system. I. Interfacial free energy. *J Chem Phys* **1958**, *28*, 258–267.
- (36) Callen, H. B. *Thermodynamics and an Introduction to Thermostatistics*; John Wiley & Sons, 2006.
- (37) Böttcher, C. *Theory of Electric Polarization*; Elsevier, 1973; pp 159 – 204.
- (38) Cahn, J. W. Critical point wetting. *J Chem Phys* **1977**, *66*, 3667–3672.
- (39) Briant, A. J.; Yeomans, J. M. Lattice Boltzmann simulations of contact line motion. II. Binary fluids. *Phys Rev E* **2004**, *69*, 031603.
- (40) Bray, A. J. Theory of phase-ordering kinetics. *Adv Phys* **1994**, *43*, 357–459.
- (41) Yang, A. J. M.; Fleming, P. D.; Gibbs, J. H. Molecular theory of surface tension. *J Chem Phys* **1976**, *64*, 3732–3747.
- (42) Evans, R. The nature of the liquid-vapour interface and other topics in the statistical mechanics of non-uniform, classical fluids. *Adv Phys* **1979**, *28*, 143–200.
- (43) Wells, G. G.; Trabi, C. L.; Brown, C. V. Fast reconfigurable liquid optical interface: investigation of higher harmonics in the periodic liquid surface wrinkle. *Micro-Optics* 2010. 2010; pp 118 – 124.
- (44) Kusumaatmaja, H.; Hemingway, E. J.; Fielding, S. M. Moving contact line dynamics: From diffuse to sharp interfaces. *J Fluid Mech* **2015**, *788*, 209–227.

- (45) Magaletti, F.; Picano, F.; Chinappi, M.; Marino, L.; Casciola, C. M. The sharp-interface limit of the Cahn–Hilliard/Navier–Stokes model for binary fluids. *J Fluid Mech* **2013**, *714*, 95–126.
- (46) Quéré, D. Rough ideas on wetting. *Physica A* **2002**, *313*, 32–46.
- (47) Wells, G.; Ruiz-Gutiérrez, É.; Le Lirzin, Y.; Nourry, A.; Orme, B.; Pradas, M.; Ledesma-Aguilar, R. Snap evaporation of droplets on smooth topographies. *Nat Commun* **2018**, *9*, 1380.
- (48) d’Humières, D.; Ginzburg, I.; Krafczyk, M.; Lallemand, P.; Luo, L.-S. Multiple-relaxation-time lattice Boltzmann models in three dimensions. *Philos Trans A Math Phys Eng Sci* **2002**, *360*, 437–451.
- (49) Fei, L.; Du, J.; Luo, K. H.; Succi, S.; Lauricella, M.; Montessori, A.; Wang, Q. Modeling realistic multiphase flows using a non-orthogonal multiple-relaxation-time lattice Boltzmann method. *Phys Fluids* **2019**, *31*, 042105.
- (50) Li, Q.; Luo, K.; Kang, Q.; He, Y.; Chen, Q.; Liu, Q. Lattice Boltzmann methods for multiphase flow and phase-change heat transfer. *Prog Energy Combust Sci* **2016**, *52*, 62–105.
- (51) Davis, P. *Interpolation and approximation*; Dover Publications, 1975.
- (52) Ginzburg, I. Generic boundary conditions for lattice Boltzmann models and their application to advection and anisotropic dispersion equations. *Adv Water Resour* **2005**, *28*, 1196–1216.
- (53) Yu, D.; Mei, R.; Luo, L.-S.; S., W. Viscous flow computations with the method of lattice Boltzmann equation. *Prog Aerosp Sci* **2003**, *39*, 329–367.
- (54) Zhang, C.; Guo, Z.; Liang, H. High-order lattice-Boltzmann model for the Cahn-Hilliard equation. *Phys Rev E* **2019**, *99*, 043310.

- (55) Guo, Z.; Zheng, C.; Shi, B. Discrete lattice effects on the forcing term in the lattice Boltzmann method. *Phys Rev E* **2002**, *65*, 046308.
- (56) Pooley, C. M.; Furtado, K. Eliminating spurious velocities in the free-energy lattice Boltzmann method. *Phys Rev E* **2008**, *77*, 046702.
- (57) Melcher, J. R.; Taylor, G. I. Electrohydrodynamics: A Review of the Role of Interfacial Shear Stresses. *Annu Rev Fluid Mech* **1969**, *1*, 111–146.
- (58) Kaatze, U. Complex permittivity of water as a function of frequency and temperature. *J Chem Eng Data* **1989**, *34*, 371–374.
- (59) Brown, C. V.; McHale, G.; Trabi, C. L. Dielectrophoresis-Driven Spreading of Immersed Liquid Droplets. *Langmuir* **2015**, *31*, 1011–1016.
- (60) Brown, C. V.; McHale, G.; Mottram, N. J. Analysis of a static undulation on the surface of a thin dielectric liquid layer formed by dielectrophoresis forces. *J Appl Phys* **2011**, *110*, 024107.
- (61) de Gennes, P.-G.; Brochard-Wyart, F.; Quéré, D. *Capillarity and wetting phenomena: drops, bubbles, pearls, waves*; Springer Science & Business Media, 2013.
- (62) McHale, G.; Brown, C.; Sampara, N. Voltage-induced spreading and superspreading of liquids. *Nat Commun* **2013**, *4*, 1605.

Graphical TOC Entry



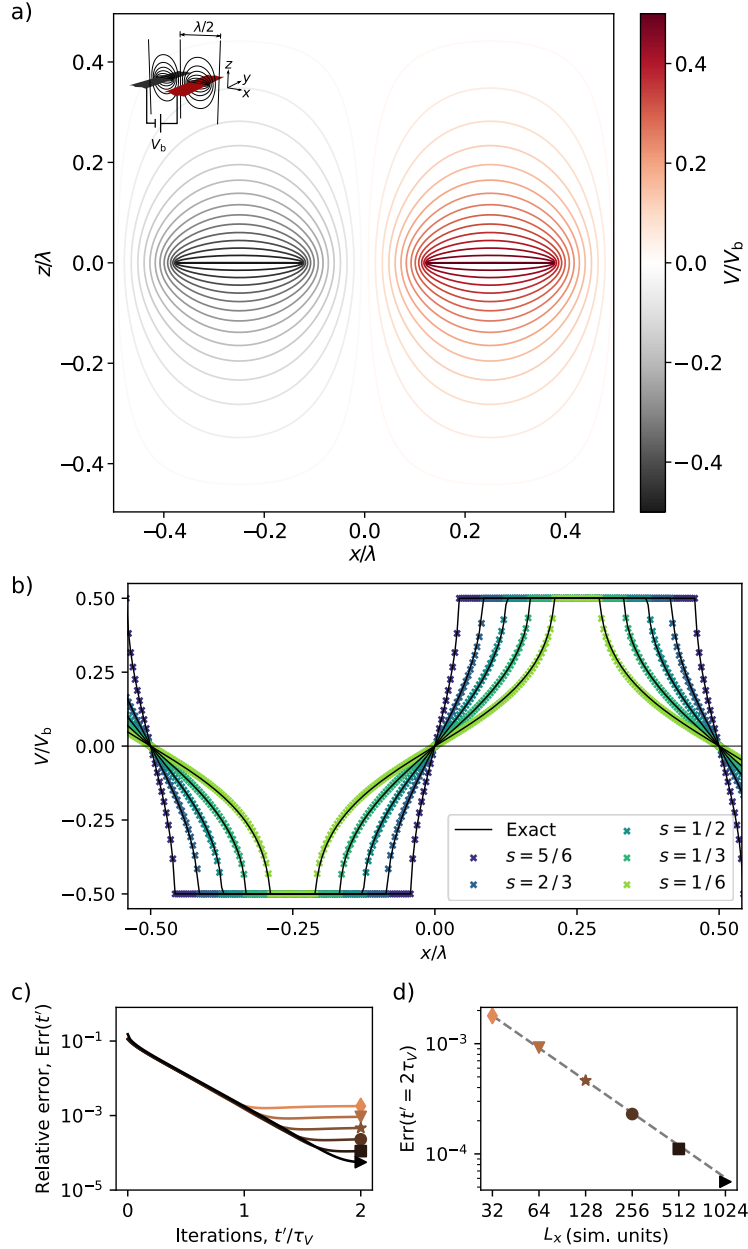


Figure 1: Electric potential of a periodic array of electrodes. (a) Equipotential lines at any xz plane obtained by the lattice-Boltzmann algorithm for an electrode configuration of equal electrode width to wavelength ratio ($s = 1/2$) and diagram of the system at the inset of the plot. (b) Comparison between the simulations against the exact solution for the profile of the electric potential at $z = 0$, $y = \text{const.}$ and varying s . (c) Relative error after $2\tau_V$ iterations for varying system size L_x . For reference, a dashed line of the slope -1 is shown under the set of points.

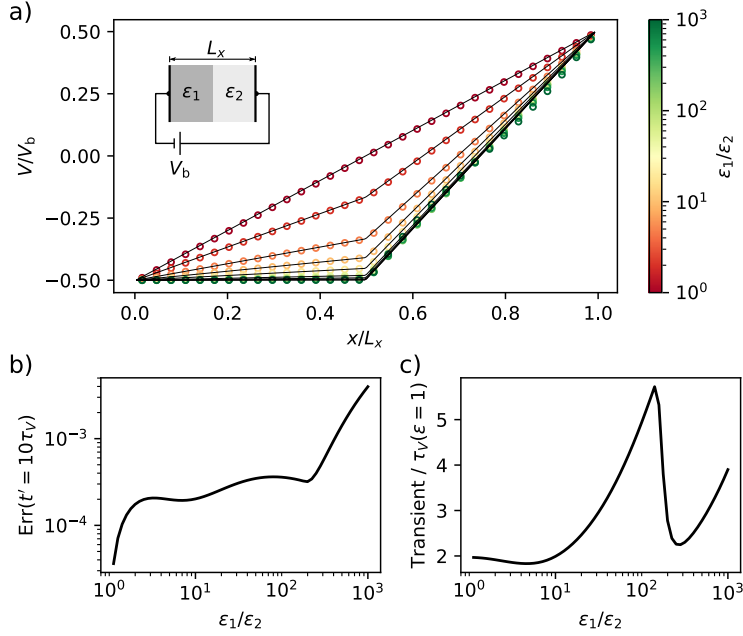


Figure 2: Profile of the electric potential of a two-dielectric capacitor. (a) Comparison between simulations (open symbols) and exact solution (solid lines) for a parallel plate capacitor of separation $L_x = 256$ in which the first half is filled by a dielectric of permittivity ϵ_1 and the second half by a dielectric of permittivity ϵ_2 held at a potential difference V_b . (b) Relative error of the algorithm against the exact solution at varying permittivity ratio. (c) Transient number of iterations compared to Eq. (42) evaluated at $\epsilon = 1$.

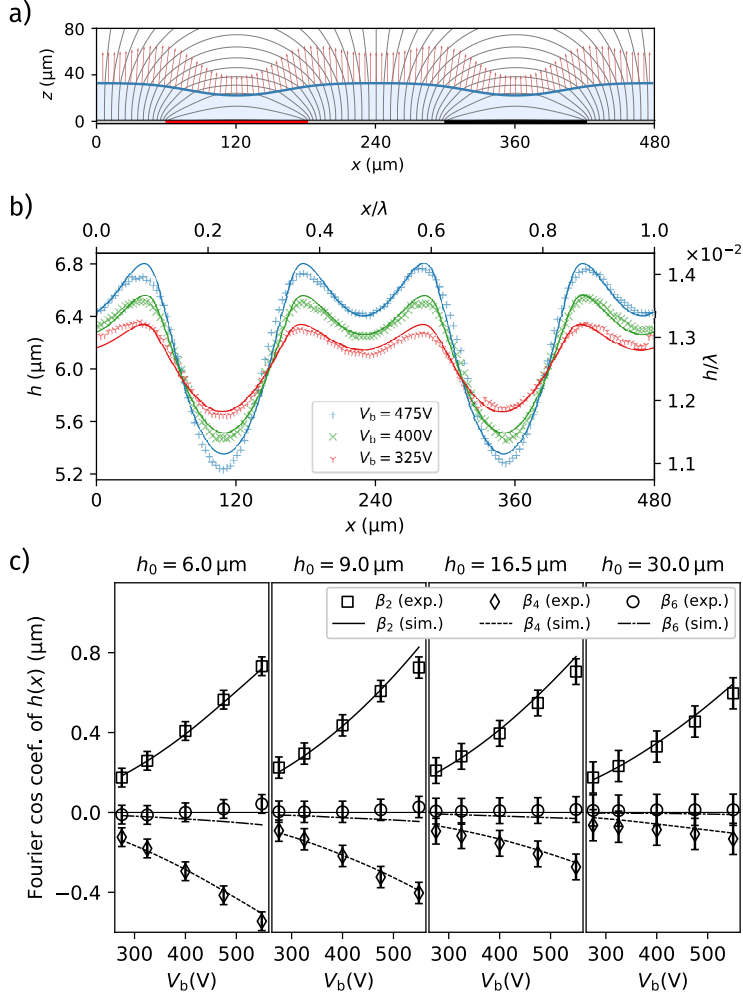


Figure 3: Wrinkling of an interface by an electric field. (a) Simulation snapshot of a dielectric liquid of thickness $h_0 = 30 \mu\text{m}$ subject to an electric field such that $\Delta\varepsilon V_b^2/2\gamma\lambda = 0.6$. The interface (solid blue line) between the stronger dielectric ($\varepsilon_1 = 2.05$, light blue area) and the weaker dielectric ($\varepsilon_2 = 1$, white area). The positive and negative electrodes (red and black lines at $z = 0$) produce an electrostatic field (shown equipotential thin lines), and the forces that wrinkle the interface (red arrows). (b) Comparison between the experimental results from Brown *et al.*, (2009)⁷ (symbols) and the present simulations (solid curves) of the profile of film of thickness $h_0 = 6 \mu\text{m}$ after the application of an electric field. (c) For a more quantitative comparison, the profile of the film can be expressed as a Fourier cosine series. The first even coefficients are plotted against the electric potential where the Fourier analysis of the experimental values (open symbols) is plotted against the simulations (solid curves).

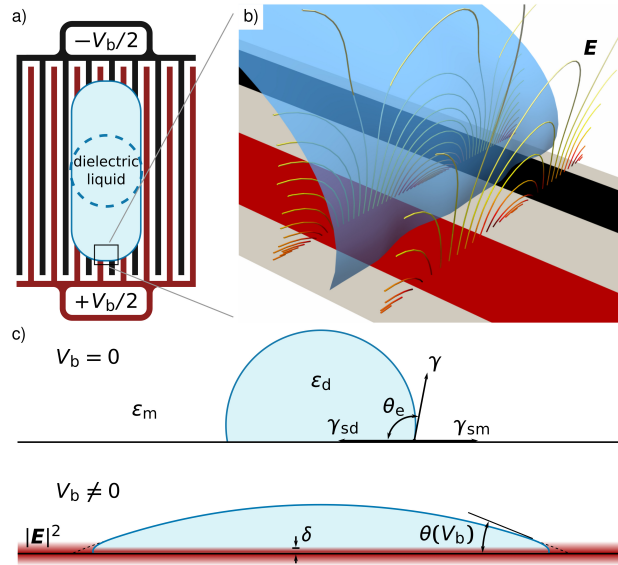


Figure 4: Illustration of the process of dielectrowetting. a) Top view of the array of interdigitated electrodes and a sessile droplet at its original (dashed line) and spread (solid line) states. b) A close up of the contact line region and the electric field (streamlines) produced by the array of electrodes. c) At $V_b = 0$, the droplet of permittivity ϵ_d and its surrounding medium of permittivity ϵ_m relax forming a contact angle of θ_e in the balance of the surface tensions γ_{sm} , γ_{sd} and γ , of the solid-medium, solid-droplet and droplet-medium interfaces. In the presence of an electric field that extends over a distance δ into the dielectric media, the droplet spreads decreasing its contact angle.

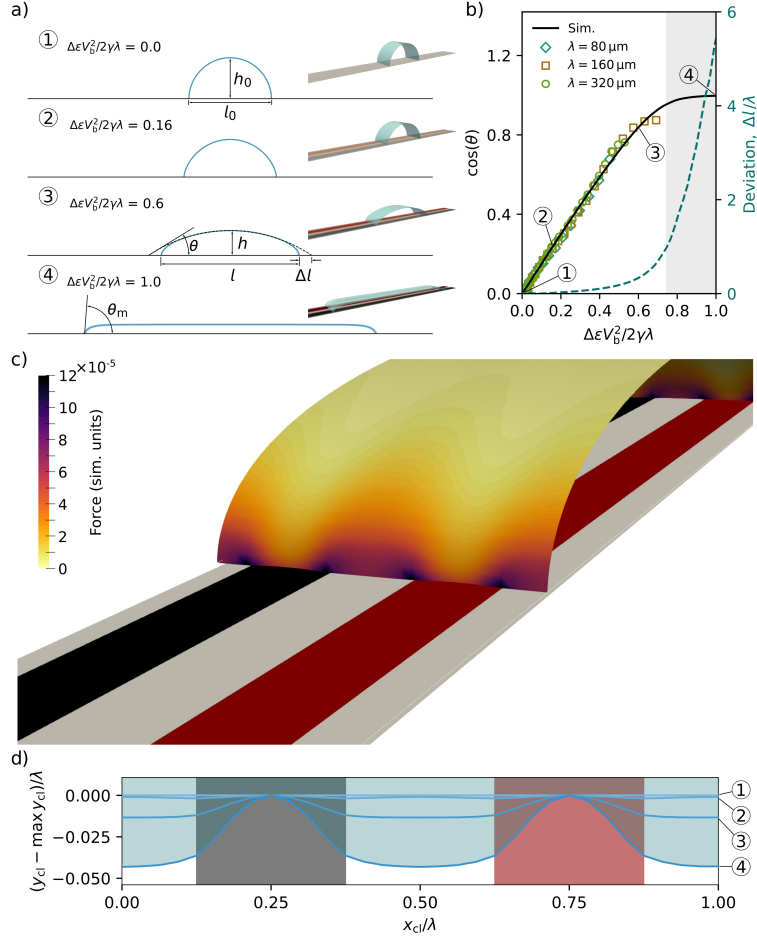


Figure 5: Spreading of a droplet by dielectrowetting. (a) Sequence of images of the quasistatic states of different voltages. The blue curve (and surface in the 3-D pictures) represents the interface of the droplet. The electrodes are shown by the red (+) and black (-) surfaces. The spreading of the droplet can also be characterised by the height-to-length ratio, h/l , to avoid the discrepancy in the circular fit and the true position of the contact line, Δl . (b) Change in the contact angle of a droplet as a function of the voltage for a simulation and the experiments of McHale *et al.* (2011)¹² and its deviation from the circular arc assumption. (c) Close up of the near-contact line region where the fluid-fluid interface is decorated by the magnitude of the dielectrophoretic force in a colour map. The simulation parameters are given in Tab. 1 and $\varepsilon_1 = 10$ and $\varepsilon_2 = 1$, for electric permittivities, and $\theta_e = 90^\circ$ for equilibrium contact angle. (d) Distortion of the contact line (solid curves), (x_{cl}, y_{cl}) , with the increase of electric potential. The blue shaded area indicates the stronger dielectric.

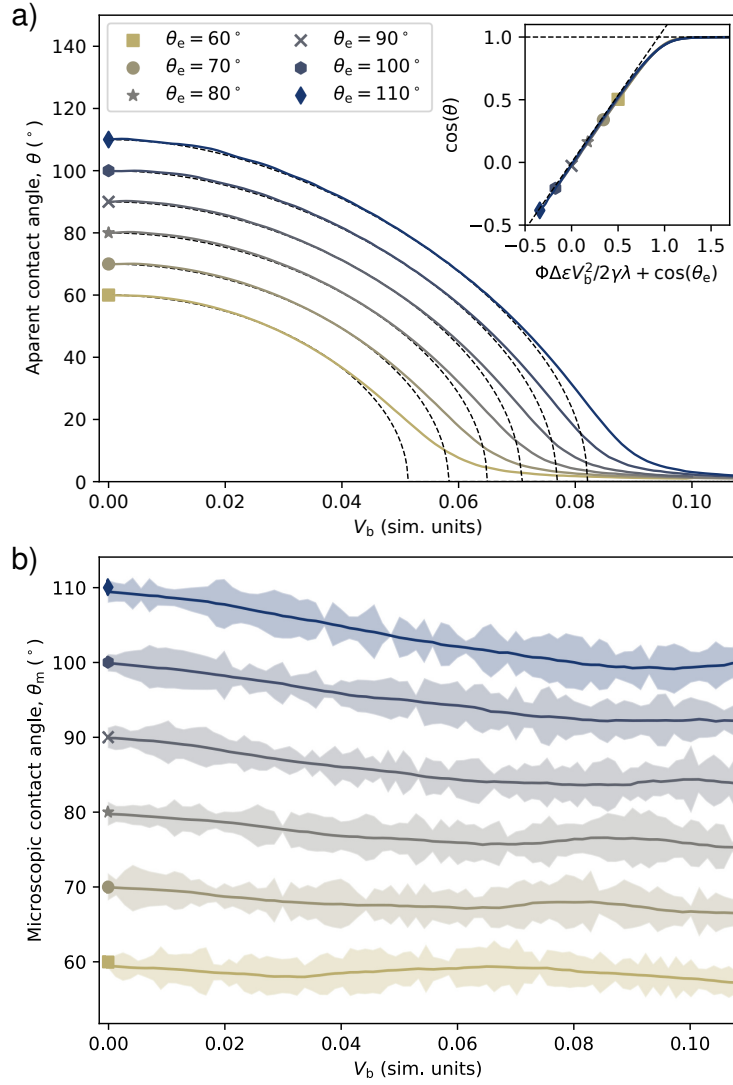


Figure 6: Simulations of the dielectrowetting of a droplet at varying equilibrium contact angle, θ_e . (a) The simulation results of the apparent contact angle, θ , as a function of the potential difference (coloured solid line) are compared against the theoretical prediction (dashed lines) of Eq. (49). Inset: The same simulation results are plotted as they appear in Eq. (49), that is, the left-hand side vs. the right-hand side of the equation. (b) Measurement of the microscopic contact angle, θ_m , as a function of the electric potential (solid lines) and the error in the measurement (shaded regions).

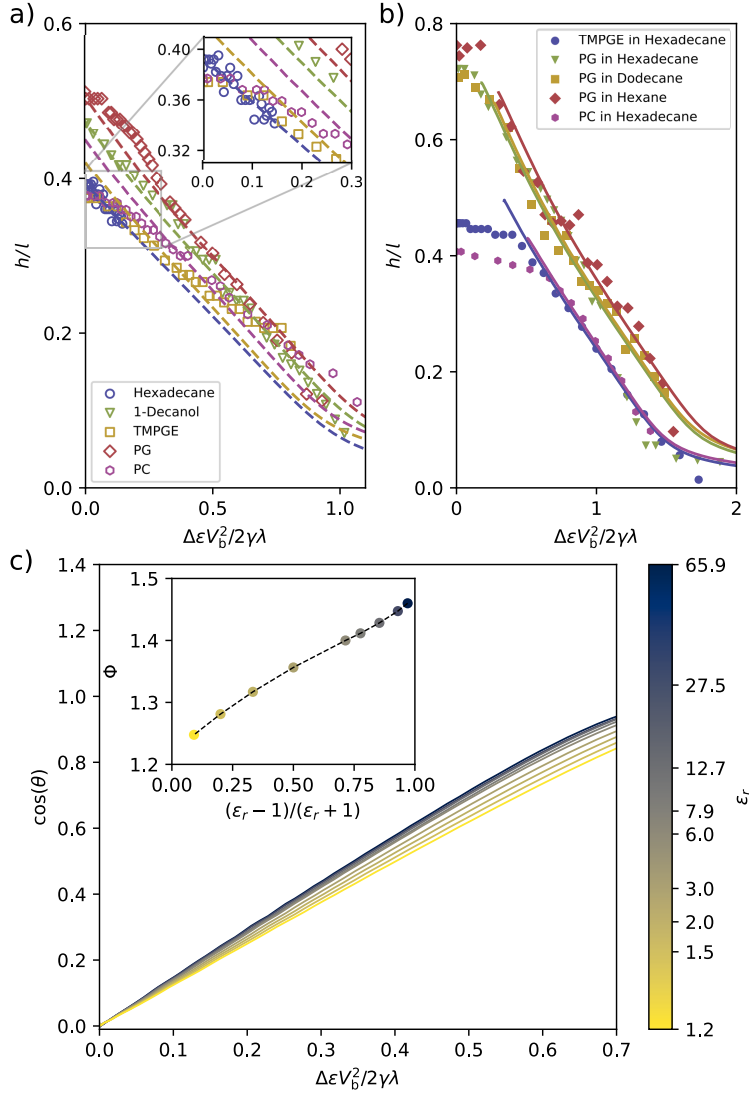


Figure 7: Effects of the electric permittivity in the spreading of a droplet. Comparison of the experimental results from Ref.⁵⁹ and the simulations of the height of a pseudo-2D droplet as a function of the electric potential at the electrodes. The experimental results correspond to two categories: (a) for a droplet surrounded by air (open symbols) and (b) by another liquid (filled symbols). The corresponding simulations for each experimental setup correspond to the dashed and solid lines of equal colour to open and filled symbols, respectively. (c) Variation of the slope of the $\cos(\theta)$ in response to the voltage squared for $\theta_e = 90^\circ$. The inset shows the dependence of the slope of these curves against the permittivity ratio. The abbreviations are PG for propylene glycol, PC for propylene carbonate and TMPGE for trimethylolpropane triglycidyl ether.